First-order vortex lattice melting in bilayer ice: A Monte Carlo method study

Telun Zhong [1], Heyang Ma [1], Peijun Zheng,[2] Jie Zhang [1,*] and Wanzhou Zhang [1,3,†]

[1]*College of Physics, Taiyuan University of Technology, Shanxi 030024, China*

[2]*Key Laboratory of Materials Physics, Institute of Solid State Physics, HFIPS, Chinese Academy of Sciences, Hefei 230031, China*

[3]*Hefei National Laboratory for Physical Sciences at the Microscale and Department of Modern Physics, University of Science and Technology of China, Hefei 230026, China*

(Received 15 April 2024; revised 16 May 2024; accepted 17 May 2024; published 25 June 2024)

Inspired by the stable bilayer water ice grown in the laboratory [Nature (London) **577**, 60 (2020)], we propose a model representing water ice as a two-layer six-vertex model. Using the loop update Monte Carlo method, we unveil meaningful findings. While the square lattice six-vertex model exhibits an antiferromagnetic to disordered phase transition known as the Berezinskii-Kosterlitz-Thouless transition, we observe a different scenario for the bilayer six-vertex model, where the transition type transforms into an Ising transition. We discover the emergence of vortices in the disordered phase, and to stabilize them, vortex excitation is induced. This leads to the presence of distinct $1/2$ filling and $2/3$ filling vortex lattice phases. More importantly, we identify the phase transitions between the vortex lattice phase and the disordered phase, as well as between the $1/2$ and $2/3$ vortex lattices, as being of first order. We also propose an experimental scheme for realizing a two-layer six-vertex model based on the artificial ice of particles in a double well trap array. Our findings provide valuable insight into the nature of phase transitions occurring in layered water ice and artificial spin or particle ice systems in experimental setups.

DOI: 10.1103/PhysRevB.109.224426

I. INTRODUCTION

Ice is a common substance in nature. There are various types of ice, including the solid form of liquid water [1], spin ice in real materials [2], artificial spin ice [3,4], and particle ice [5]. One common feature of the different forms of ice is the ice rule, i.e., the so called two-in (close) two-out (far away) topological constraint, introduced by Pauling in 1935 [6]. Water ice exhibits 19 stable geometric structures, currently identified through high pressure and low temperature experiments [1]. Spin ice also exists many real materials with different structures, such as rare-earth pyrochlores $Ho_2Ti_2O_7$ [7].

Researchers have also attempted to grow artificial spin ices [8], due to their controllability. The microscale systems used to create artificial spin ice typically involve magnetically interacting nanoislands or nanowire links [9], superconducting-qubit arrays [10]. The physics studied through ice is very broad; it covers residual entropy [11], frustration [2], monopoles [12], and so forth.

Artificial spin ice can construct various configurations, including the vortex lattice (VL) phase [13]. Its periodic structure composed of vortices is called the VL. As vortex states can help understand superconductors [14], many studies have been done on transitions between vortex lattices and other phases [15–18]. In the XY model, the unbinding of the vortex-antivortex pairs is considered the cause of the Berezinskii-Kosterlitz-Thouless (BKT) phase transition [19–21]. However, the vortex lattice leads to a first-order phase transition in the real crystals YBCO and $YBa_2Cu_3O_7$ [15–18].

Of course, the ice physics can also be explored through experiments with water ice. In 2020, the group at Peking University confirmed the existence of two-dimensional two-layered water ice [22]. The positions of the upper layer oxygen ions, as well as the connections between the oxygen ions, are exactly the same as those in the lower layer, i.e., AA stacking ice. Such a stable structure of water was first predicted in 1997 using a molecular dynamics simulation [23]. Actually, there exists another type of ice with an AB stacking structure [24] as shown Fig. 1. There is a relative 180 degree rotation between the two layers, which are connected by hydrogen bonds. Alternatively, the hydrogen bonds of the first layer are shifted onto the faces of the second layer. It has been confirmed to be stable under reasonable temperatures and pressures by *ab initio* calculations [24] though lacking in experimental preparation [22].

To inspire experimental physicists to achieve AB or other types of bilayer ice in the future, we further convert the bilayer ice to the bilayer six-vertex (6V) model [25]. On the basis of the bilayer square lattice 6V model, the AB stacking honeycomb 6V model can be formed by bending one leg of the vertices to the appropriate degree. Hydrogen ions and oxygen ions in ice can be close to each other or far apart, similar to the situation of spin-up and spin-down. Viewing ice as a spin system helps understand the phase transitions between different types of ice under various conditions like temperature and pressure. *It is not clear whether or not there is something new in the bilayer honeycomb 6V model.*

In this paper, we apply a large-scale loop Monte Carlo (MC) simulation to study the proposed 6V model. By

*Contact author: zhangjie01@tyut.edu.cn

†Contact author: zhangwanzhou@tyut.edu.cn

properly defining and scanning the type and weight, including the vortex exciting weight, we explore the phase diagrams systematically. The system includes ferromagnetic, antiferromagnetic, 1/2-filling VL, 2/3-filling VL, and disordered phases. The theoretically discovered types of phase transitions, such as first-order phase transitions, also provide insight into understanding previous experiments [15–18].

The outline of this work is as follows. Section II introduces the bilayer 6V model, algorithm, and the measured quantities. Section III describes the phase diagram and details without the effects of vortex weight $V = 1$. Section IV describes the phase diagram with the effects of vortex weight $V \neq 1$. Section V discusses the experimental realization. Conclusive comments and outlook are made in Sec. VI.

Physically, apart from the bilayer 6V model initially proposed, we have made new discoveries as follows.

(I) The transition between the antiferromagnetic phase to the disordered phase is of Ising type for our bilayer 6V model. However, for the 6V model on the square lattice, the transition is of BKT type [26].

(II) Two types of vortex lattice phase are found when vortex excitation is induced. The transition from vortex lattice phases to other phases is of first order, consistent with previous crystal experiments [15,16] . This helps researchers understand that not all phase transitions involving vortices are BKT phase transitions.

On the algorithmic level, although Ref. [25] has simulated the single-layer planar 6V model using the loop algorithm, our model is the nonplanar 6V model and we provide the details of closing loops. In addition, we introduce a Metropolis type short-loop update method for the purpose of ergodicity.

Experimentally, bilayer water ice, where the ordering is due to the proton positions [22], is probably better captured by particle-based ice [5]. Here, we propose to groove or imprint both bilayer lattices onto a single-layer substrate, and each edge of the lattices are realized by a double well trap with only one particle.

II. MODEL, ALGORITHM, AND QUANTITIES

A. The 6V model with vortex weight

1. Hamiltonian and partition function

Unlike the models such as the Ising [27], XY [19–21], Potts [28] models, or the coupled spins such the Ising-XY model [29], etc., the famous 6V model does not have a explicit Hamiltonian. However, each type of vertex has its own weight and can also have an equivalent energy, and the vertex satisfies the "two-in-two-out" topological constraints. For convenience, to measure physical quantities related to specific heat and other energy-related quantities, a quasi-Hamiltonian is introduced as

$$\mathcal{H} = -\sum_{i=1}^{2N} \epsilon_i - v \sum_{j=1}^{2f} n_i, \tag{1}$$

where $-\epsilon_i$ is the effective energy for each vertex labeled by i, and $-v$ is a local vortex energy for each plaquette. n_i represents the number of vortices in each plaquette, where $n_i = 1$ denotes a clockwise ↻ or a counterclockwise ↺ vortex, and $n_i = 0$ signifies the absence of a vortex. N is the total number of vertices of one layer and f is the total number of faces of the honeycomb lattice of one layer.

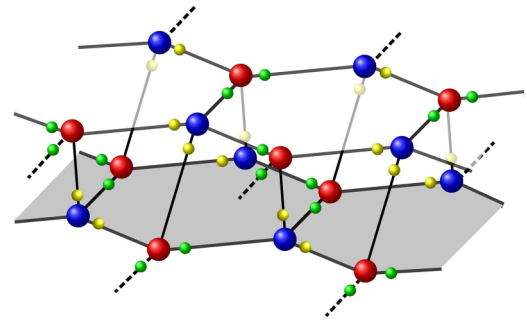

FIG. 1. The construction of the two-layer ice model. The large balls (in red and blue) represent O^{2-}s and the small balls denote H^{+}s. The different colors for the large ball means AB stacking [24]. The "two-in-two-out" rule can be demonstrated by the small balls in different colors.

Using the Boltzmann weight factor, the vertex weight is

$$\omega_i = \exp(\beta\epsilon_i) \tag{2}$$

and the vortex weight is

$$V_i = \exp(\beta v n_i), \tag{3}$$

where $\beta = 1/k_B T$ is the inverse temperature and set to 1, and the partition function of the system is defined as follows:

$$\mathcal{Z} = \prod_{i=1}^{2N} \omega_i \prod_{j=1}^{2f} V_j. \tag{4}$$

Figures 2(a1)–2(c2) show the configurations of six vertices, and each vertex has four legs marked by the red arrows. The directions of the legs satisfy two of them facing out away from the center and two legs pointing toward the center. For simplicity, the weights of the six vertices take values as

$$w_i = [a, a, b, b, c, c]. \tag{5}$$

Here, the flipping symmetry of the leg direction is considered, i.e., the state of (a1) can be obtained by flipping the directions of the four legs of (a2), and therefore the weights of these two vertices are the same as a. In total, only three possible weight values a, b and c are needed for the six different configurations. This tradition is also used in Ref. [26].

2. The formation of two-layer honeycomb lattice structure

Figures 2(d1)–2(e2) show how to use the vertices to construct two-layer honeycomb lattices. Firstly, 6V models are usually constructed in the two-dimensional plane, and it is rare to see two-layer 6V models. Here, the interlayer coupling is realized by connecting the two vertices, using the two red legs marked 2, 4 in the vertical direction. Then, the second step rotates the two legs (in blue) to the horizontal y direction. A small coordinate axes system denoted x, y, z is shown for reference.

It is also essential to illustrate the relationship between the two-layer honeycomb 6V model and the structure of ordered water molecules. In Figs. 2(f1) and 2(f2), the arrows

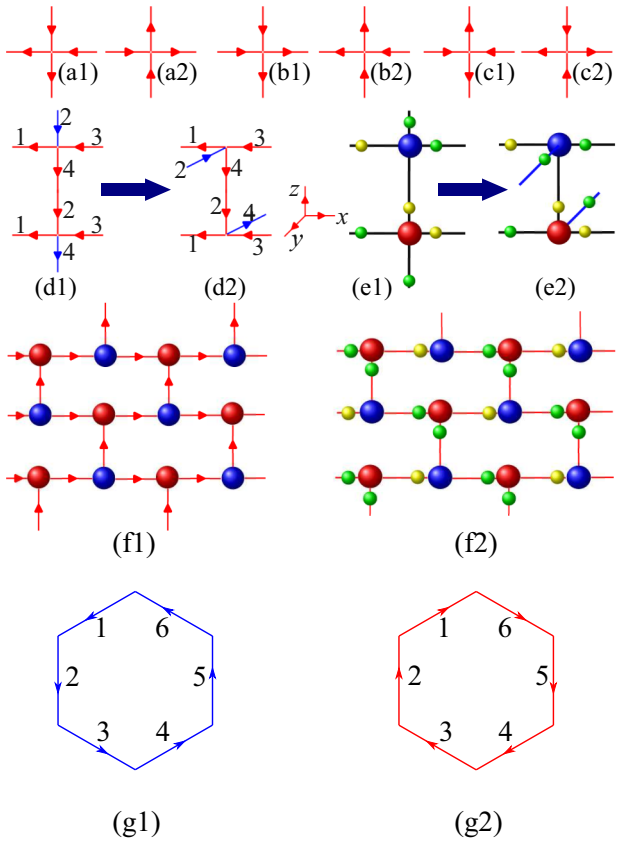

FIG. 2. Schematic diagram of the 6V model and water molecules. [(a1)–(c2)] The configurations of six vertices and their weights defined as a, a, b, b, c, and c, respectively. [(d1) and (d2)] Connecting the two vertices by the two vertical red legs marked by 2 and 4. [(e1) and (e2)] Rotating the two legs, marked in blue, on the horizontal plane. [(f1) and (f2)] Mapping to the structure of real water ice molecules. The small ball represents the hydrogen ion and the large ball represents the oxygen ion. [(g1) and (g2)] The definition of the vortex.

pointing towards the center of the vertex corresponds to the approaching of the hydrogen (H) ions towards the oxygen (O) ion in a real water molecule. Conversely, arrows pointing away from the center indicate that the hydrogen ions stay away from the oxygen ion. Ultimately, the arrangement of vertices can describe the structure of real water ice molecules.

It should be noted that the vortex is defined as shown in Figs. 2(g1) and 2(g2). Numerically, the requirement is that the angle difference between adjacent vectors is $\frac{\pi}{3}$, i.e.,

$$\theta_{\mathrm{mod}\{i,6\}+1} - \theta_i = \pi/3, \tag{6}$$

where i ranges from 1 to 6. This type of definition does not need the saw function in Ref. [29] and is the same as the one in Ref. [30].

In addition, the configurations of the system also depend on the topological constraints of "two-in-two-out" rules [25,31]. In other words, the arrows in the vertices have two pointing of them to the center and the other two back to the center. The real configurations of large lattices need to be simulated by various MC methods [32,33], which will be discussed in the next section.

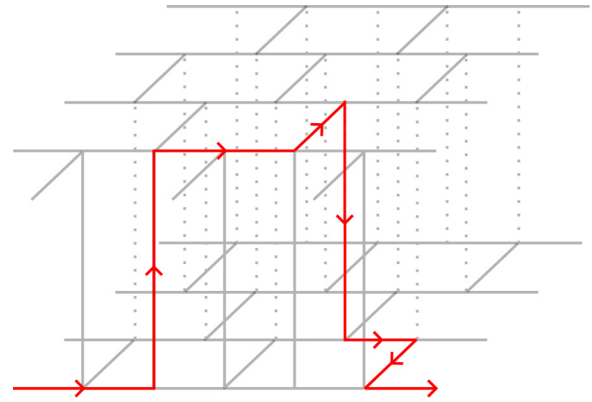

FIG. 3. Schematic diagram of the loop algorithm in a two-layer honeycomb lattice. The starting point is selected randomly, and the red arrows illustrate the path of the process. When the head of the loop meets the start vertex, the loop is closed and the configuration is updated. For convenience in defining the coordinates of the vertices, the honeycomb is defined as a topologically equivalent brick wall structure.

B. Methods and the measured quantities

1. Methods

In this paper, we apply the loop algorithm, which has proven effective in studying various systems both classical systems systems [25], and quantum systems [25,34]. A similar loop algorithm is the famous worm algorithm [35,36], which involves a partial loop with two open ends with very efficient dynamical behaviors [37]. The 6V model is very similar to the flow representation of other models [38–40].

To execute a loop update, the following steps are performed as shown in Fig. 3.

(1) First, we initialize the system with $N = 2L_x \times L_y$ vertices, and then randomly select one of the vertices. Next, we randomly choose one of the four legs of the vertex to place the head of the loop.

(2) The leg where the head of the loop is located is used as the entrance leg, and then again one of the four legs from that vertex is chosen as the exit leg with a certain probability.

(3) The head of the loop enters the next new vertex, and the exit leg of the previous vertex is connected to this new vertex.

(4) To continue the process, we repeat steps 2 and 3 until the head of the loop and the end of the loop meet. Additionally, as the head of the loop traverses each leg, the state (arrows) of that leg should be flipped.

Let's explain how to choose the exit leg when the loop head has been determined. Here, we employ the Metropolis-Hastings strategy. Suppose the weight of the reference vertex is w_0, and the weights of the new vertices resulting from exiting from the four legs are w_1, w_2, w_3, and w_4, respectively. We choose a random number between 0 and 1 to determine the interval in which the random number falls. These intervals are defined as $[0, p_1]$, $(p_1, p_1 + p_2]$, $(p_1 + p_2, p_1 + p_2 + p_3]$, and $(p_1 + p_2 + p_3, 1]$, where the probabilities are defined as

$$p_i = w_i / \sum_{i=1}^{4} w_i. \tag{7}$$

TABLE I. Parameters a, b, and c, and the possible range of bounce probability p_a, p_b, and p_c, where the subscripts a, b, c represent the vertices of type a, b, c that the loop encounters during its walk.

$a+b$	$\lvert a-b\rvert$	c	p_a	p_b	p_c
<1	\	1	$(0, \frac{1}{2})$	$(0, \frac{1}{2})$	$(\frac{1}{2}, 1)$
\	>1	1	$(0, \frac{a}{a+1})$	$(0, \frac{b}{b+1})$	$(\frac{1}{a+b+1}, \frac{1}{2})$

If the outgoing and incoming legs are exactly the same, then there is no update, and the corresponding probability p is referred to, as the bounce probability. Generally, a higher bounce probability leads to lower efficiency of the loop algorithm [25,34].

Therefore, analyzing the possible range of bounce probabilities under different parameters (see Table I) would be helpful to ensure the feasibility of the code.

Loop close is an important step in the loop algorithm. In some cases, the length of the loop is very big and the code consumes very long run times. The authors of Ref. [41] even cut the loop by the so-called short-loop methods.

Here, we resort to the method dealing with the quantum Bose-Hubbard models [42–45]. Two ways of closing loops are used. In Fig. 4(a), the beginning leg is labeled by "first" and the ending leg is marked by "last." In this case, the first and the last legs meet (overlap) at the same leg, and then the loop closes. In Fig. 4(b), the last leg connects to the position of the initial leg. This constraint arises from the "2-in and 2-out" condition, allowing the loop closure only when connected to the initial leg. The distinction lies in the fact that in the former case, the vertex labeled "1" undergoes two updates, whereas in the latter, it undergoes only a one time update.

2. The measured quantities

(Ia) The magnetization in the x direction is

$$M_x^{\pm} = \sum_{i,j} (\pm 1)^{i+j} S_{i,j}^x / N, \tag{8}$$

where (± 1) denotes the phase factor of ferromagnetization (FM) or antiferromagnetization (AFM), respectively. The symbol x refers to the horizontal directions of the lattice, and

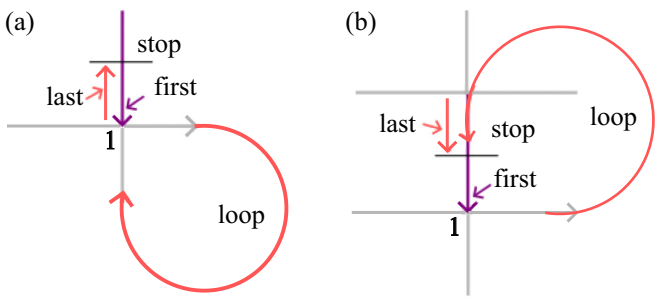

FIG. 4. The two ways in which the loops close. (a) The first and last legs overlap at the same leg, and (b) the last leg connecting to the first leg but the two legs belong to a pair of neighborhood vertices.

TABLE II. The four phases and their boundaries in terms of the parameters a, b, c, and Δ.

Phase	Δ	$a,\ b,\ c$	m_x^+	m_x^-
FM	$\Delta > 1$	$b-a>c$	1	0
FM	$\Delta > 1$	$a-b>c$	1	0
DIS (D)	$-1 < \Delta < 1$	$a+b>c$	0	0
AFM	$\Delta < -1$	$a+b<c$	0	1

i and j mean the coordinates of the vertices in the x and y directions.

(Ib) The absolute values of magnetizations are

$$m_x^{\pm} = \langle |M_x^{\pm}| \rangle, \tag{9}$$

where $\langle\rangle$ signifies the averages of Monte Carlo simulations.

(Ic) The striped ferromagnetization is defined as

$$m_s = \sum_{i=1}^{L} \left| \sum_{j=1}^{L} S_{i,j}^x \right| / N, \tag{10}$$

which is used later to define the striped specific heat C_{ms}.

(Id) The Binder ratios are also defined as

$$Q = \langle (M_x^-)^2 \rangle^2 / \langle (M_x^-)^4 \rangle \tag{11}$$

$$Q_s = \langle m_s^2 \rangle^2 / \langle (m_s)^4 \rangle, \tag{12}$$

corresponding to the antiferro magnetization M_x^- and the striped ferromagnetization m_s, respectively.

(II) Vortex density

$$\rho_{vx} = \frac{1}{2f} \sum_{i=1}^{2f} n_i, \tag{13}$$

where f is the total number of faces of one layer.

(III) Specific heats C_V, and C_{vx} are expressed as

$$C_V = \frac{2N}{k_B T^2} [\langle e^2 \rangle - \langle e \rangle^2], \tag{14}$$

$$C_{vx} = \frac{2N}{k_B T^2} [\langle \rho_{vx}^2 \rangle - \langle \rho_{vx} \rangle^2], \tag{15}$$

where e is the average energy per site. C_V and C_{vx} are specific heats related to energy and vortex.

III. PHASE DIAGRAM $V = 1$ ($v = 0$) AND DETAILS

A. Global phase diagram with $V = 1$

We first consider the global phase diagram with the vortex-excitation factor $V = 1$. Traditionally, for a two-dimensional square lattice with periodic boundary conditions, the variable Δ was introduced to describe the phase diagram [25,31],

$$\Delta = \frac{a^2 + b^2 - c^2}{2ab}, \tag{16}$$

and the four phases, along with their boundaries expressed in terms of the parameters a, b, c and Δ, are listed in Table II.

In Fig. 5(a), the four phases are depicted, where the ferromagnetic (FM) phase, the antiferromagnetic (AFM) phase, and the disordered (D) phase are schematically located in

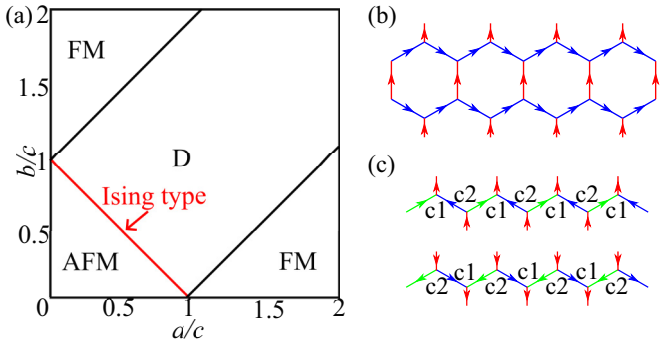

FIG. 5. Global phase diagram in the plane $(a/c - b/c)$ with $V = 1$ and snapshots. (a) Phase diagram containing AFM, FM, and disordered phases (b) the typical snapshot in the FM phase. The AFM-D transition is of Ising type. (c) Two configurations of the AFM phase for the Z2 symmetry breaking.

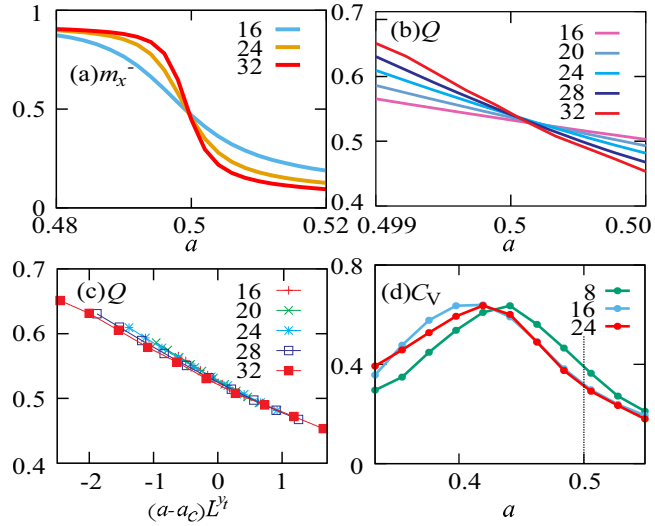

FIG. 6. Different quantities scanning a while keeping $a = b$ (a) m_x^- (b) Q (c) Data collapse of Q, while using $y_t = 1$. (d) Repeating C_V of the F model on the square lattice [26].

Figs. 5(b)–5(d), respectively. For simplicity, we only show snapshots from the lower layer of the 6V model; the features of the other layer can be inferred based on symmetry.

Surprisingly, the phase diagram of the six-vertex model on our bilayer honeycomb lattice is identical to the tabulated results in Table II from the square lattice presented above [25,31].

One may wonder why the two-layer 6V model is the same as the single-layer square lattice 6V model. Let us now briefly analyze a few locations of the phase transition boundary. The first point is $(a/c, b/c) = (1, 0)$ which is the point of phase transition between the AFM and FM phases. As illustrated in Fig. 5(a), the FM-phase is full of vertices with weight a and the AF-phase is full of vertices with weight c. At the point of phase transition of the two phases, i.e., phase AFM and phase FM, free energies are equal and defined by the following:

$$N_a \ln a - T S_{\rm FM} = N_c \ln c - T S_{\rm AFM}, \tag{17}$$

$N_a = N_c = 2L^2$, where $S_{\rm AF}$ and $S_{\rm FM}$ are the entropies of the two phases, respectively,

$$S_{\rm FM} = S_{\rm AFM} = k_B \ln 2. \tag{18}$$

Along the $b = 0$ axis, the system in the FM phase only has either all a1 type vertices or all a2 type vertices. In other words, there are two microscopic states. Similarly, in the AFM phase, there exist configurations with only all c1 or all c2 type vertices. Therefore $a/c = 1$ is the critical point satisfying Eq. (17) at $b = 0$.

B. Ising type not BKT type in transition along $a = b$

The phase transitions of the 6V model are identical on both the square lattice and the double-layer honeycomb lattice. For example, along $a = b$, Ref. [26] confirms the critical point is at $\beta_c = \ln(2)$. The critical point locates at

$$a_c = b_c = 1/2. \tag{19}$$

In our MC simulation, as shown in Figs. 6(a)–6(b), the intersection of m_x^- and its Binder ratio Q locates at $a_c = b_c = 1/2$.

However, the type of the phase transition changes. In the F model, the phase transition belongs to be the BKT type, as evidenced by the nondivergent behavior of specific heats in Fig. 4 in Ref. [26]. In our bilayer 6V model, the type should be of Ising type.

The first signal is that, for the Ising phase transition, the critical exponent $y_t = 1$. Using the finite size scaling equation defined as follows:

$$Q = Q_0 + e_1(T - T_c)L^{y_t} + e_2(T - T_c)^2 L^{2y_t} + \cdots + f_1 L^{y_1} + f_2 L^{y_2} + \cdots, \tag{20}$$

and the data collapse method, Q is plotted as function of $(a - a_c)L^{y_t}$, and data of different sizes overlap as shown in Fig. 6(c). This phenomenon supports the conclusion that the observed phase transition is indeed the Ising type.

This type of Ising phase transition can also be analyzed from the perspective of symmetry breaking. In the AFM phase, as depicted in Fig. 5(c), there is a twofold degeneracy in the configuration. In the horizontal direction, one configuration is characterized by a c1-c2-c1-c2 vertex arrangement, while the other features a c2-c1-c2-c1 arrangement. Moreover, the relationship between these two configurations is achieved by flipping the states of all legs. This means that from disorder to AFM, there is a Z2 symmetry breaking leading to the Ising transition.

To further vindicate our code, we also simulate the F model on the one-layer square lattice; the C_V indeed does not diverge at a_c as shown in Fig. 6(d), consistent with the result in Ref. [26].

IV. PHASE DIAGRAM WITH $V \neq 1$

In this section, we introduce a nonzero value for v in Eq. (1) to discuss the effects of vortex excitation.

As in Ref. [30], it is experimentally possible to manually insert or delete vortices [46,47], despite the fact that the factors are added manually here.

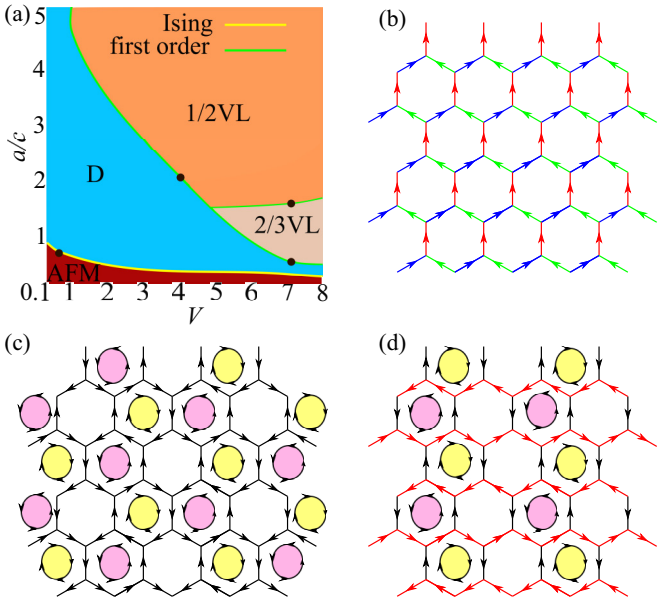

FIG. 7. Global phase diagram with $V \neq 1$ and snapshots. (a) A schematic phase diagram (b) the AF phase (c) 2/3 VL phase (d) 1/2 VL phase. In fact, 1/2 VL is accompanied by a x-direction ferromagnetic order and 2/3 VL is accompanied by an AFM order (see Appendix A).

This phase diagram is shown in the a-V plane, where $V = e^{v}$, while simultaneously maintaining a fixed cut along $b = a$.

A. Global phase diagram

Figure 7(a) shows the global phase diagram, which contains the AFM, disordered, 1/2 and 2/3 VL phases. When the vortex excitation is considered, the phase diagram becomes rich in features. In Fig. 7(c), the configuration of the 2/3-VL phase is shown. The dual lattice of the honeycomb lattice is the triangular lattice. In this phase, two of the three sets of sublattices within the triangular lattice are occupied by positive and negative vortices, respectively, while the remaining set of sublattices contains no vortices. In Fig. 7(d), the configuration of the 1/2-VL phase is shown. In this phase, positive and negative vortices alternate sequentially along the y direction, forming connected stripes.

Here, we analyze the distribution of different phases within the phase diagram. When a and b are very small, $a = b \ll c$ and $V \ll c$, the system resides in the AFM phase, represented by the dark red region. In the upper right region, $a = b \gg c$ and $V \gg c$, the system corresponds to the 1/2 VL phase. The system has almost no type c vertices. At the same time V drives the system to form vortices consisting of vertices of type a, b only, as shown in Fig. 17(a).

When $a = b \in [0.5c, 2c]$, the influence of V drives the system to form vortices consisting of vertices of types a, b, and c, maintaining a 1:1:1 ratio, and the typical configuration of 2/3 VL phase is illustrated in Fig. 17(b).

In the disordered phase, the characteristics of vortices vary across different parameter regimes. As depicted in Fig. 17(e), two distinct regimes are identified, labeled as ③ and ④.

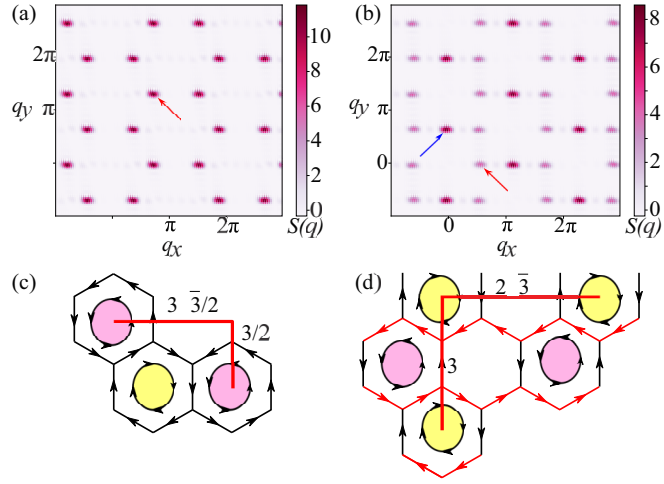

FIG. 8. The vortex structure factor $S(\boldsymbol{q})$ defined in Eq. (21) for (a) 2/3 VL and (b) 1/2 VL phases in $\boldsymbol{q}$ space. The translation vectors in real space (c) 2/3 VL and (d) 1/2 VL phases.

In the region where $V < 1$ and $a(b)$ is large, as shown in Fig. 17(c), vortices are absent. The reason is that a vortex typically requires the presence of vertices of types a, b, and c, within its structure. Conversely, in the other regime where $V > 1$ and reasonable values of $a(b)$ are considered, as illustrated in Fig. 17(d), numerous vortices appear randomly throughout the system.

In fact, 1/2 VL is accompanied by a x-direction ferromagnetic order and 2/3 VL is accompanied by an AFM order (see Appendix B).

B. Vortex structure factors

To further understand the spin vortex lattice phase, the structure factor in $\boldsymbol{q}$-space is introduced as

$$S(\boldsymbol{q}) = \frac{1}{N_c} \sum_{i,j} e^{i\boldsymbol{q}\cdot(\boldsymbol{r}_i - \boldsymbol{r}_j)} \langle n_i n_j \rangle, \tag{21}$$

where n_i, n_j represents 1, 0, in the face of the honeycomb lattices, i.e., a triangular lattice. The symbols $\boldsymbol{r_i}$ and $\boldsymbol{r_j}$ are the center coordinates of the vortex. In real space, if the density obeys configurations of the form $(101010\cdots)$ or $(010101\cdots)$, the wave vector corresponding to the maximum value of $S(\boldsymbol{q})$ should be located at $\boldsymbol{q} = (\pi, 0)$ [48].

In Fig. 8(a), for the 2/3 VL phase, $S(q_x, q_y)$ is obtained by using Eq. (21) with a lattice size $L = 12$. One of the brightest points is located at

$$(q_x, q_y) = \left(\frac{4\sqrt{3}}{9}\pi, \frac{4}{3}\pi\right), \tag{22}$$

as indicated by the red arrow. The position of the peaks reflects the translational symmetry of the vortex lattice. Assuming that the side length of the honeycomb lattice is 1, the spacing between the two pink vortices $\boldsymbol{r_i}$ and $\boldsymbol{r_j}$ is:

$$\Delta x = x_i - x_j = 3\sqrt{3}/2 \tag{23}$$

and

$$\Delta y = y_i - y_j = 3/2. \tag{24}$$

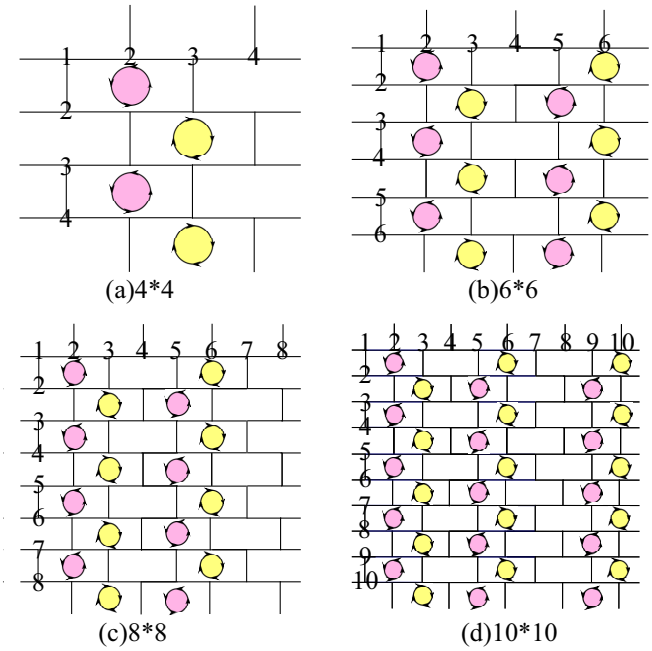

FIG. 9. Vortex and anti-vortex in the lattices with $L = 4,\ 6,\ 8,$ and 10.

The position in Eq. (22) can be obtained by using

$$q_{x(y)} = 2\pi/\Delta x(y). \tag{25}$$

For the 1/2 VL lattice, $S(q_x, q_y)$ is shown in Fig. 8(b). The brightest point (as indicated by the blue arrow) is located at

$$(q_x, q_y) = \left(0, \tfrac{2}{3}\pi\right), \tag{26}$$

and the second brightest point (as indicated by the red arrow) is located at

$$(q_x, q_y) = \left(\frac{\sqrt{3}}{3}\pi, 0\right). \tag{27}$$

This is because in real space, the translation vectors are respectively $\Delta x = 2\sqrt{3}$ and $\Delta y = 3$.

In total, we have identified two VL phases in the bilayer 6V model with vortex weight where $V > 1$. These ordered states can be distinguished by examining either their respective structure factors or the relevant order parameters.

C. Size effects from periodic boundaries

Figure 9 shows the size effects of the vortex density in a 2/3 VL with $L = 4,\ 6,\ 8,$ and 10. The honeycomb lattice is a complex lattice with two sites in its smallest cell, hence having an even number of lattice sites in the horizontal direction, i.e., $L \bmod 2 = 0$.

In Fig. 9(a), for $L = 4$, each row contains two faces, one of which is occupied by a vortex. The vortex density, i.e., the ratio between the number of vortices and faces, is $\rho_v = N_v/N_f = 1/2$. Similarly, for $L = 6,\ 8,$ and 10, the densities become $\rho_v = 2/3,\ 2/4,$ and 3/5, respectively, as shown in Figs. 9(b)–9(d). In Table III, we list some possible small sizes and vortex densities.

TABLE III. The table shows the maximum theoretical value of the vortex density ρ_v as a function of system size L.

Phase	L	4	6	8	10	12	14	16	18	20	L
2/3 VL	ρ_{vx}	1/2	2/3	2/4	3/5	4/6	4/7	5/8	6/9	6/10	$\frac{\lfloor L/3\rfloor}{L/2}$
1/2 VL	ρ_{vx}	1/2	1/3	2/4	2/5	3/6	3/7	4/8	4/9	5/10	$\frac{\lfloor L/4\rfloor}{L/2}$

For more general sizes, the densities are as follows:

$$\rho_v = \frac{\lfloor L/3\rfloor}{L/2}, \tag{28}$$

where the symbol $\lfloor . \rfloor$ denotes rounding down. We first explain Eq. (28) using $L = 6$, two sites labeled as 1, 2 in the horizontal direction, a total of $L/2$ bricks in each row as shown in the denominator.

Then we explain the numerator in Eq. (28). The following three subequations explain the number of vortices corresponding to the three sizes L, $L + 2$, and $L + 4$, as shown below:

$$\frac{L}{2} \times \frac{2}{3} = \frac{L}{3} \to \frac{L}{3} = \left\lfloor \frac{L}{3} \right\rfloor, \tag{29a}$$

$$\frac{L+2}{2} \times \frac{2}{3} = \frac{L}{3} + \frac{2}{3} \to \frac{L}{3} = \left\lfloor \frac{L+2}{3} \right\rfloor, \tag{29b}$$

$$\frac{L+4}{2} \times \frac{2}{3} = \frac{L}{3} + \frac{4}{3} \to \frac{L}{3} + 1 = \left\lfloor \frac{L+4}{3} \right\rfloor, \tag{29c}$$

equation where $L + 2$ in Eq. (29b) indicates two additional sites compared to L, i.e., a new empty face without a vortex ($n_i = 0$), as illustrated by comparing Figs. 9(b) and 9(c) in the first lines.

Through the analysis above and the densities presented in Table III, in the 2/3 VL phase, the density remains constant for sizes where $L \bmod 6 = 0$. Therefore, when observing physical quantities later on, we only simulate systems whose size is a multiple of 6.

D. Detailed transitions between the phases

In this section, our focus is on examining the specific details of phase transitions between multiple phases, and analyzing its underlying reasons.

1. The Ising transition between the AFM and disordered phases at $V < 1$

Initially, we scan the parameter $a = b \in [0.5, 0.8]$ at $V = 0.5$, around the black point in the lower left corner of the phase diagram. Various quantities are shown in Fig. 10.

In Figs. 10(a) and 10(b), the specific heat C_V and C_{vx} exhibit divergence with respect to sizes during the phase transition between the AFM and disordered phases. This behavior stands in contrast to the *convergence* of C_V in the single-layer 6V F model [26], as shown in Fig. 6(d).

In Figs. 10(c) and 10(d), the Binder cumulant Q, along with its data collapse at the critical point $a_c = 0.617$, yields $y_t = 1$, providing additional confirmation of the Ising transitions.

The possible reasons of the Ising transition between the AFM and disordered phases at $V < 1$. Be precise are as follows: $V < 1$ implies the absence of the disordered phase as

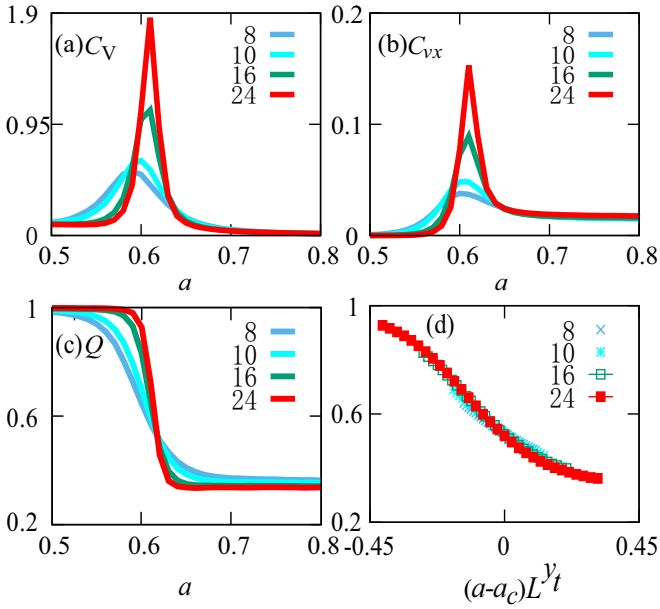

FIG. 10. The Ising transition between the AFM and disordered phases at $V < 1$, $a = b$ and $V = 0.5$. (a) C_V, (b) C_{vx}, and (c) Q (d) data collapse of Q, using $y_t = 1$. The system size ranges from 8 to 24.

depicted by the absence of vortices in Fig. 17(c). Additionally, the AFM phase has no vertex, as illustrated in Fig. 7(d). Consequently, the phase transition between these two phases does not involve vortices. Moreover, the transition from simple AFM order to disorder involves $Z2$ symmetry breaking.

2. Transitions between the D and 1/2 VL phases at $V > 1$

The phase transition between disordered and the 1/2 VL phase is discussed. By fixing the parameter $V = 4$, and scanning a and keeping $a = b$, the vortex density ρ_{vx}, and C_V are measured for different sizes $L = 16$–48.

As shown in Figs. 11(a) and 11(b), the jumps of ρ_{vx} and peaks of C_V show the signatures of phase transitions. The divergence of C_V confirms the phase transition is not of BKT type [30]. In Figs. 11(c) and 11(d), the histograms of E/N and m_s are obviously double peaked at the parameters $a = b = 2$. This indicates the phase transition is of first order.

The signature of the first order transition can also obtained by fitting the critical exponent. Using the package for finite size scaling [49], ν is obtained as 0.48(8) using Eq. (20).

The data for sizes $L = 32,\ 36,$ and 40 overlap very well. The scaling dimension $y_t = 1/0.48 = 2.08 \approx 2$ equals to the system dimension $d = 2$ when the first-order transition occurs [50].

3. Transition between the D and 2/3 VL phases

The transition from the 2/3 VL phase to the disorder phase is also first order. In Figs. 12(a) and 12(b), the double peaks in the distribution of $P(E)$ and $P(\rho_{vx})$ indicating a first-order phase transition.

Different from the 1/2 VL phase as shown in Fig. 11, this phase transition has an obvious size effect. Figure 12(c) illustrates that the specific heat peak shifts to the right as the

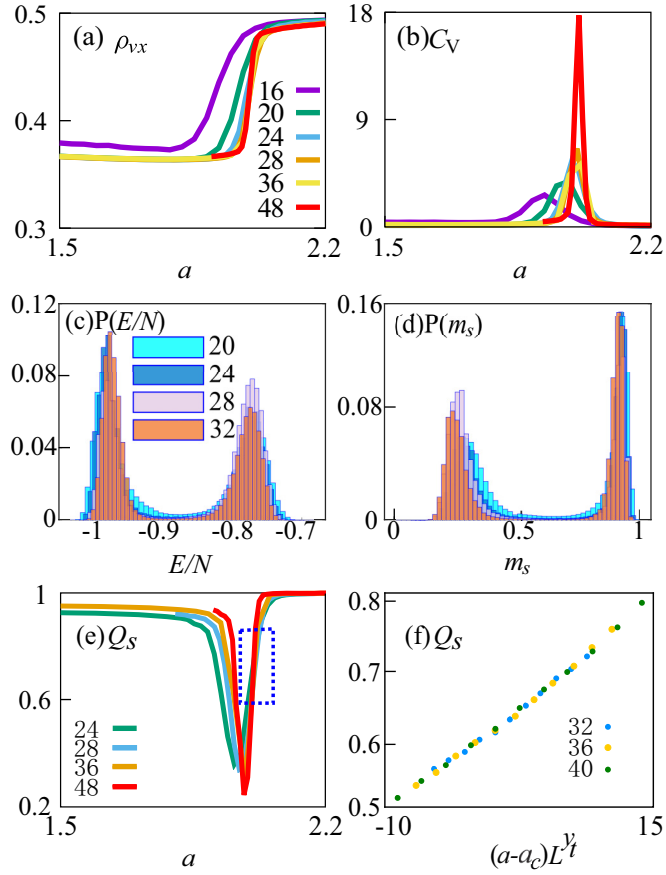

FIG. 11. The signatures of the first-order phase transition at $V = 4$. The quantities (a) ρ_{vx} (b) C_V with system sizes $L = 16$–48. The double peaked distributions (c) $P(E/N)$ and (d) $P(m_s)$ at $a = 2.004(1)$. (e) Q_s and (f) data collapse of Q_s and obtaining $\nu = 0.48(8)$ [49].

size increases. Fortunately, through finite-size scaling defined as follows:

$$a_c(1/L) = K/L + a_c(L = \infty), \tag{30}$$

the position of the specific heat converges under the thermodynamic limit $a_c(L = \infty) = 0.475811(2)$. The line $a_c(1/L)$ versus $1/L$ is shown in Fig. 12(d).

The error bar (2) from 0.475811(2) is calculated by the following equations. First, if one fits $y = kx + b$, then the standard deviation of the intercept b is

$$s_b = \sqrt{\frac{n}{n\sum_i^n x_i^2 - \left(\sum_i^n x_i\right)^2}} \times s_y \tag{31}$$

where n is the number of points involved, s_y is the standard deviation of the observation y_i and can be expressed as

$$s_y = \sqrt{\frac{\sum_i^n (y_i - kx_i - b)^2}{n-2}}, \tag{32}$$

where $n - 2$ is the degree of freedom. If one fits the data using "gnuplot" software, the result is $a_c(\infty) = 0.476(5)$ consistent with the above result within the error bar.

To show that the results are convergent, Fig. 12(e) displays E/N versus MC steps. The converging time is about 10^6 steps.

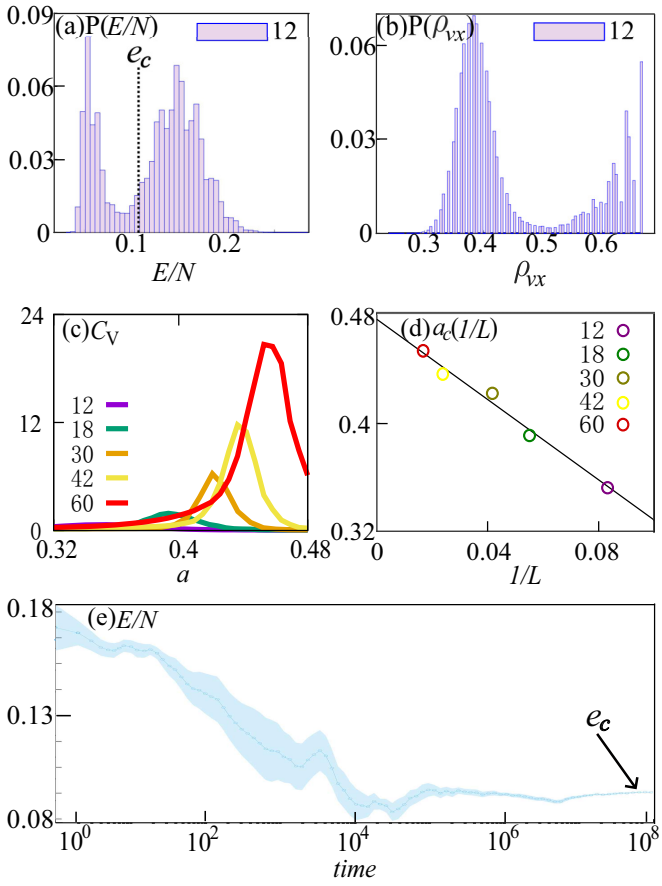

FIG. 12. The signatures of the first-order phase transition. The double peaked distributions of (a) $P(E/N)$ and (b) $P(\rho_{vx})$ at $V = 7$ and $a = 0.35$. (c) C_V vs a, (d) a_c vs $1/L$. (e) E/N versus MC steps and the convergent time is about 10^6.

The converged energy is approximately 0.12 and denoted as e_c which is also marked by a dashed line in Fig. 12(a), sitting between the two peaks.

4. First-order transition between the two vortex lattice phases

Similar to the atomic solid phase in the classical limit [42–45] for the BH model, the phase transition between 1/2 VL and 2/3 VL phases, should be of first order. The exact boundary between these two phases can be obtained analytically by comparing the free energy $F = E - TS$ of both phases.

By convention, the temperature is set to be $T = 1$. By careful checking, the entropy for both phases is respectively $S_{1/2} = \ln 64$ and $S_{2/3} = \ln 36$. The entropy does not depend on the lattice size, and therefore, the average entropy for per site denoted as $S/L^2/2$ should be zero in the thermodynamic limit $L \to \infty$. The energies of the two phases are defined as follows:

$$E_{1/2\mathrm{VL}} = -L^2 \ln a - L^2 \ln b - \tfrac{1}{2} L^2 \ln V$$

$$E_{2/3\mathrm{VL}} = -\tfrac{2}{3} L^2 \ln a - \tfrac{2}{3} L^2 \ln b - \tfrac{2}{3} L^2 \ln c - \tfrac{2}{3} L^2 \ln V,$$

where $-L^2 \ln a - L^2 \ln b$ and $-\frac{2}{3} L^2 \ln a - \frac{2}{3} L^2 \ln b - \frac{2}{3} L^2 \ln c$ are the vertex energies for both phases, and $-\frac{1}{2} L^2 \ln V$ and $-\frac{2}{3} L^2 \ln V$ are the energies for the vortex. Let

$$F_{1/2\mathrm{VL}} = F_{2/3\mathrm{VL}}, \tag{33}$$

while keeping $a = b$, the reduced analytical expression becomes

$$a^4 = V, \tag{34}$$

when $L = \infty$.

Numerical simulations are also performed to confirm the first-order transition between the vortex phases. In Fig. 13(a), the distributions of ρ_{vx} for the sizes $L = 12$ and 24 are obtained. In Fig. 13(b), the curves ρ_{vx} versus L are plotted. The gray data are MC results with 20 independent bins. The theoretical a_c, are marked by the red line to guide the eyes.

In the regime of a strong first-order transition, the cluster algorithm encounters the issue of ergodicity. As a result, we have also incorporated the Metropolis type short-loop update scheme. The short loop in the z-direction is composed of four vertices, with each vertex contributing two legs that form the rectangles depicted in Fig. 11(c). These pairs of legs are (3,4), (2,3), (1,2) and (4,1), respectively. In order to keep the "two-in-two-out" constraint, we flip eight legs simultaneously with a certain probability without violating the "ice" rule for each involved vertex. During the actual simulation, after each round of loop updates, we check if there are any short loops present. If a short loop is found, we attempt to flip it.

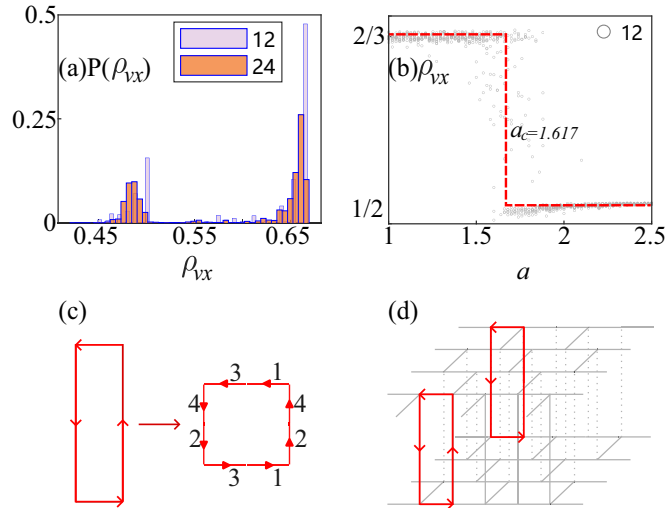

FIG. 13. Signal of the first-order phase transition. (a) The double peaked distribution of ρ_{vx}, with $V = 7$, $a = 1.68$ (b) ρ_{vx} vs a (c) a short loop in the vertical direction, and the numbers 1, 2, 3, 4 represent the legs. (d) The Metropolis type short-loop updating.

5. Effect of temperature gradient field

On the single-layer honeycomb lattice, vortex lattice has been achieved using the charged colloidal particle-based ice numerically [51]. The Coulomb repulsion between charged particles favors vortices at low temperatures. Experimentally, a magnetic colloidal particle [52] inside lithographically sculptured double well traps, with tunable repulsive interactions of magnetic moments, also favors vortices.

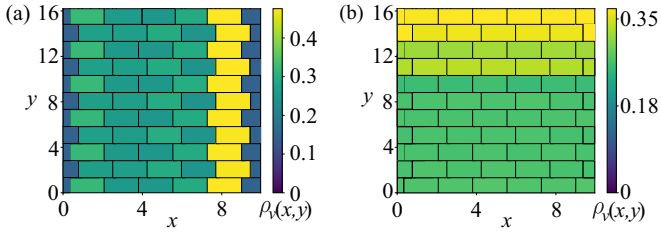

FIG. 14. The distribution of vortex density $\rho_v(x, y)$ with temperature gradient field (a) along the x direction and (b) along the y direction. The temperature varies from 1 to 0.45 with an interval of 0.05, with $a = b = 1.5,\ c = 1,\ V = 2$ at the site (1,1).

However, raising the temperature [51] results in the vortex state melting into a disordered state. Additionally, introducing a magnetic field [53] or an electric field in the plane also easily transitions the vortex state into a ferromagnetic state.

Another factor of the vortex depinning is a temperature gradient field. Here we put a temperature field distributed on the lattice, with the temperature decreasing. The pattern of vortex density $\rho_v(x, y)$ becomes striped as shown in Figs. 14(a) and 14(b). The vortex density $\rho_v(x, y)$ at higher temperature region are larger than that in the lower temperature region. Specifically, the coordinate variables $x_1, x_2, \ldots, x_L$ are mapped to $T_1, T_2, \ldots, T_L$, and ultimately to $a_1, a_2, \ldots, a_L$ by $a_i = b_i = \exp(\epsilon_i/T_i)$. A similar mapping applies to the vortex weight V_i.

Note that before applying the temperature gradient field, we set the temperature to 1. Then, we calculate the energy of each vertex in the lattice based on parameters a, b, c and the Boltzmann weight. When introducing the temperature gradient field, it's crucial to maintain these energies fixed, as vertices at different positions experience different temperatures.

When an external field is applied, vortices either disappear or form stripes. Without an external field, due to translational invariance, the vortex density is uniformly distributed. The different average distributions of vortex density with and without an external field indicate vortex depinning.

V. EXPERIMENT REALIZATION USING PARTICLE BASED ICE

The colloidal particle-based ice, as discussed in Ref. [54], is another system capable of realizing bilayer ice, in addition to water ice, natural spin ice, and artificial spin ice. The theoretical concept behind colloidal particle ice involves employing elongated optical traps to confine colloidal particles. Each optical trap features two wells where colloidal particles can reside. These arrays of traps can organize into different kinds of lattices [51,54,55]. Additionally, the presence of topological charges [56], vortex states [57] and skyrmions patterns [58], boundary effects [59], can be simulated by particle-based ice. More complete reviews are present in Ref. [5].

Experimentally, bilayer water ice, where the ordering is due to the proton positions [22], is probably better captured by particle-based ice [5]. Particle-based systems could include charged or magnetic colloids interlacing in an array that mimics spin ice and more closely resembles the water ice's proton ordering despite their different natures [53]. The implementation of a two-well trap array embedded in a substrate has been achieved in references [52,60,61], on two-dimensional lattices. However, for a bilayer lattice, achieving the required structure has not yet been accomplished.

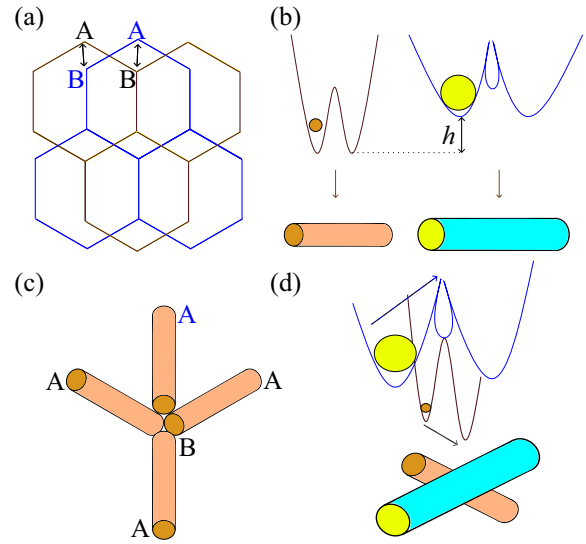

FIG. 15. The method of embedding the A-B stacked bilayer honeycomb lattice into the single-layer substrate (a) The single-layer rendition of two honeycomb lattices, with double-sided arrows indicating their connection. (b) Representation of two different double well traps for the two lattices, each accommodating a single colloidal particle. These traps can be symbolized as bonds. (c) Illustration of the "two-in-two-out" rule pattern, where site B connects four A sites, including one A site from a different lattice. (d) Depiction of crossing bonds and their corresponding double well structures.

Here, we propose imprinting both layers onto a single-layer substrate, as schematically illustrated in Fig. 15(a). The upper and lower honeycomb lattices are depicted in blue and black, respectively. Interlayer connections are denoted by double arrows. Given that this is an A-B stacked bilayer, the sites on the A sublattice and the B sublattice are connected pairwise.

As depicted in Fig. 15(b), each edge can be represented as a double well holding only one colloid. Some edges corresponding to the two layers intersect, raising the possibility of particle collision at these intersections. To reduce this, the depths of the two wells can be adjusted differently. The black wells are deep, while the blue ones are shallow. Additionally, a small well between the two blue wells helps the passage of small colloids.

In Fig. 15(c), the arrangement illustrates four noncrossing bonds. Site B (in the lower layer) connects to four A sites, with the blue A site originating from the upper layer. In Fig. 15(d), the crossing bonds are depicted. The shallow and deep wells meet at the intersection from different directions. Both the big and small colloids can move within their respective wells.

VI. DISCUSSION AND CONCLUSION

In this paper, we model two-dimensional two-layer water ice as a two-layer 6V model. By means of the loop update Monte Carlo method, we obtain interesting results.

Our study contrasts the square lattice 6V model, where the AFM to the disordered phase transition is governed by the BKT mechanism, with the bilayer 6V model, characterized by a conventional Ising phase transition due to Z2 symmetry breaking. We find that the transitions from vortex lattice phases to the disorder phase and between different vortex lattice phases are both of first order. This insight advances our understanding of the phase transitions present in layered water ices, contributing to the broader comprehension of complex systems in physics.

Despite conducting numerous simulations, there are still many open questions.

(i) As an initial investigation, we assumed $a = b$, and the case where $a \neq b$ has not been studied yet. The exploration of vortex glass induced by random values of a, b, and V worthwhile. Furthermore, the disorder we observed can potentially be further classified into disordered structures with vortices and disordered structures without vortices.

(ii) For the bilayer water ice [22], the systems have various types of boundaries, such as zigzag and armchair edges, and rough random edges. It is interesting to simulate the bilayer honeycomb 6V model with different boundaries.

(iii) Although we are not clear about how water ice regulates the ratios of a, b, and c types of vertices, it is possible to artificially adjust them in the case of artificial spin [3] or particle ice [5], which is rich in physical properties.

(iv) Regarding the numerical methods for studying this model, not only are conventional MC methods suitable, but tensor network methods [62] are also well-suited for exploring this model. There are existing literature studies that have employed tensor network methods to investigate similar models such as the dimer model and the ice model [63]. However, in our case, we introduce a slightly more complex factor by incorporating vortex weighting, which results in an increase in the bond dimensions of the tensors.

ACKNOWLEDGMENTS

We thank Vladimir Korepin and Tzu-Chieh Wei for their inspiration regarding the six-vertex model, and Youjin Deng, Chengxiang Ding, and Tony C. Scott of RWTH-Aachen University for commenting on the manuscript, and valuable suggestions from the reviewers. This work was supported by the Hefei National Research Center for Physical Sciences at the Microscale (KF2021002), and the Shanxi Province Science Foundation (Grants No. 202303021221029 and No. 202103021224051).

APPENDIX A: DESCRIPTION OF THE BOUNCE PROBABILITIES

In Sec. II B, Table I shows the range of bounce probabilities p_a, p_b and p_c. In this Appendix, more details are described.

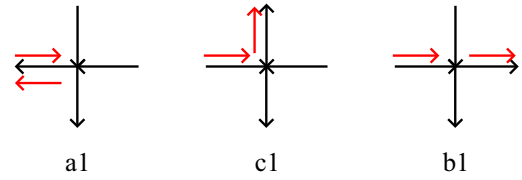

FIG. 16. Two allowable exit legs and one bounce leg for the 6V model.

Corresponding to the 6V model, the general expression of the bounce probability of the loop algorithm is

$$p_i = \frac{w_i}{w_a + w_b + w_c}, \tag{A1}$$

where the denominator is the sum of the weights of the three vertices after the loop passes through two allowable exit legs and one bounce leg (Fig. 16), and the numerator w_i are the weights of the vertices encountered during the loop walk. The subscript i denotes types of a, b, or c. To discuss the range of p_i, it is only necessary to discuss the maximum and minimum values of Eq. (A1), where the variable w_c is already fixed to 1. Taking $p_a \in (0, 1/2)$ in the AFM phase as an example, the weights w_a and w_b are independently adjustable, but they meet the range $0 < a + b < 1$, and therefore the maximum value of $p_a = a/(a + b + 1) \to a/(a + 1) \to 1 - 1/(a + 1) = 1/2$.

APPENDIX B: CONFIGURATIONS WITH THE *a*, *b*, *c* TYPES VERTICES AND VORTICES

In Figs. 17(a)–17(d), the snapshots of the configurations with vertices and vortices are shown. The parameters chosen correspond to the positions marked as ①, ②, ③, ④ in Fig. 17(e).

In the 2/3 vortex lattice phase, not only do vortex orders exist but also AFM orders with a length of 3 in the x direction, Fig. 17(f). If $y == 1$, $S_{y,x} = 1$ for $x \in [1, 2, 3]$ and $S_{y,x} = -1$ for $x \in [1, 2, 3]$. The definition to quantify such a pattern is as follows:

$$M_3 = \sum_{i=1}^{L} \left| \sum_{j=1}^{L} (-1)^{\lfloor (j-1)/3 \rfloor} S^x_{i,j} \right| / N, \tag{B1}$$

where $\lfloor (j-1)/3 \rfloor$ means replacing 1,2,3,4,5 and 6 to 0,0,0,1,1, and 1. Similarly, for the 1/2 VL lattice, there is a FM order in the x direction and the quantity is defined in Eq. (10).

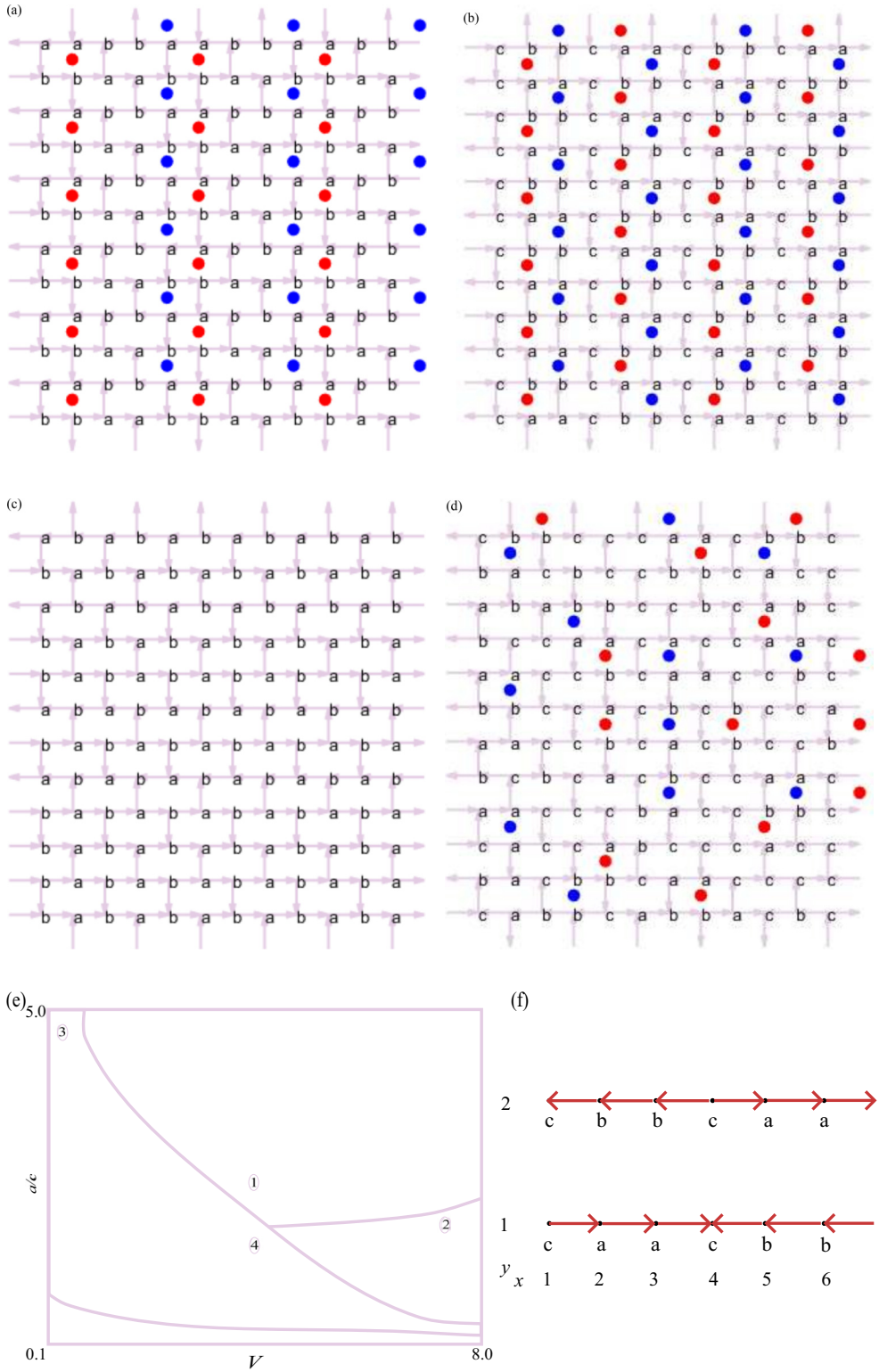

FIG. 17. Snapshots for different phases. (a) $\rho_v = 1/2$ striped vortex lattice, (b) $\rho_v = 2/3$ vortex lattice, (c) disordered phase without vortex, (d) disordered phase with vortex, and (e) the four snapshots are obtained at parameters marked in ①, ②, ③ and ④. (f) The AFM pattern with minimum unit length 3 on the 2/3 VL lattice.

[1] C. G. Salzmann, J. S. Loveday, A. Rosu-Finsen, and C. L. Bull, Structure and nature of ice XIX, Nat. Commun. **12**, 3162 (2021).

[2] S. T. Bramwell and M. J. P. Gingras, Spin ice state in frustrated magnetic pyrochlore materials, Science **294**, 1495 (2001).

[3] S. H. Skjrv, C. H. Marrows, R. L. Stamps, and L. J. Heyderman, Advances in artificial spin ice, Nat. Rev. Phys. **2**, 13 (2020).

[4] C. Nisoli, R. Moessner, and P. Schiffer, Colloquium: Artificial spin ice: Designing and imaging magnetic frustration, Rev. Mod. Phys. **85**, 1473 (2013).

[5] A. Ortiz-Ambriz, C. Nisoli, C. Reichhardt, C. J. O. Reichhardt, and P. Tierno, Colloquium: Ice rule and emergent frustration in particle ice and beyond, Rev. Mod. Phys. **91**, 041003 (2019).

[6] L. C. Pauling, The structure and entropy of ice and of other crystals with some randomness of atomic arrangement, J. Am. Chem. Soc. **57**, 2680 (1935).

[7] M. J. Harris, S. T. Bramwell, D. F. McMorrow, T. Zeiske, and K. W. Godfrey, Geometrical Frustration in the Ferromagnetic Pyrochlore $Ho_2Ti_2O_7$, Phys. Rev. Lett. **79**, 2554 (1997).

[8] W.-C. Yue, Z. Yuan, Y.-Y. Lyu, S. Dong, J. Zhou, Z.-L. Xiao, L. He, X. Tu, Y. Dong, H. Wang, W. Xu, L. Kang, P. Wu, C. Nisoli, W.-K. Kwok, and Y.-L. Wang, Crystallizing kagome artificial spin ice, Phys. Rev. Lett. **129**, 057202 (2022).

[9] R. F. Wang, C. Nisoli, R. S. Freitas, J. Li, W. McConville, B. J. Cooley, M. S. Lund, N. Samarth, C. Leighton, V. H. Crespi, and P. Schiffer, Artificial 'spin ice' in a geometrically frustrated lattice of nanoscale ferromagnetic islands, Nature (London) **439**, 303 (2006).

[10] A. D. King, C. Nisoli, E. D. Dahl, G. Poulin-Lamarre, and A. Lopez-Bezanilla, Qubit spin ice, Science **373**, 576 (2021).

[11] A. Ramirez, A. Hayashi, R. Cava, R. Siddharthan, and B. Shastry, Zero-point entropy in 'spin ice', Nature (London) **399**, 333 (1999).

[12] C. Castelnovo, R. Moessner, and S. Sondhi, Magnetic monopoles in spin ice, Nature (London) **451**, 42 (2008).

[13] M. L. Latimer, G. R. Berdiyorov, Z. L. Xiao, F. M. Peeters, and W. K. Kwok, Realization of artificial ice systems for magnetic vortices in a superconducting MoGe thin film with patterned nanostructures, Phys. Rev. Lett. **111**, 067001 (2013).

[14] J.-Y. Ge, V. N. Gladilin, J. Tempere, V. S. Zharinov, J. Van de Vondel, J. T. Devreese, and V. V. Moshchalkov, Direct visualization of vortex ice in a nanostructured superconductor, Phys. Rev. B **96**, 134515 (2017).

[15] V. K. Vlasko-Vlasov, J. R. Clem, A. E. Koshelev, U. Welp, and W. K. Kwok, Stripe domains and first-order phase transition in the vortex matter of anisotropic high-temperature superconductors, Phys. Rev. Lett. **112**, 157001 (2014).

[16] B. Maiorov, G. Nieva, and E. Osquiguil, First-order phase transition of the vortex lattice in twinned $YBa_2Cu_3O_7$ single crystals in tilted magnetic fields, Phys. Rev. B **61**, 12427 (2000).

[17] E. Zeldov, D. Majer, M. Konczykowski, V. B. Geshkenbein, V. M. Vinokur, and H. Shtrikman, Thermodynamic observation of first-order vortex-lattice melting transition in $Bi_2Sr_2CaCu_2O_8$, Nature (London) **375**, 373 (1995).

[18] T. Sasagawa, K. Kishio, Y. Togawa, J. Shimoyama, and K. Kitazawa, First-order vortex-lattice phase transition in $(La_{1-x}Sr_x)_2CuO_4$ single crystals: Universal scaling of the transition lines in high-temperature superconductors, Phys. Rev. Lett. **80**, 4297 (1998).

[19] J. M. Kosterlitz and D. J. Thouless, Long range order and metastability in two dimensional solids and superfluids. (Application of dislocation theory), J. Phys. C: Solid State Phys. **5**, L124 (1972).

[20] J. M. Kosterlitz, Nobel Lecture: Topological defects and phase transitions, Rev. Mod. Phys. **89**, 040501 (2017).

[21] V. Berezinsky, Destruction of long range order in one-dimensional and two-dimensional systems having a continuous symmetry group. I. Classical systems, J. Exp. Theor. Phys. **32**, 493 (1970).

[22] R. Ma, D. Cao, C. Zhu, Y. Tian, J. Peng, J. Guo, J. Chen, X.-Z. Li, J. S. Francisco, X. C. Zeng, L.-M. Xu, E.-G. Wang, and Y. Jiang, Atomic imaging of the edge structure and growth of a two-dimensional hexagonal ice, Nature (London) **577**, 60 (2020).

[23] K. Koga, X. C. Zeng, and H. Tanaka, Freezing of Confined Water: A Bilayer Ice Phase in Hydrophobic Nanopores, Phys. Rev. Lett. **79**, 5262 (1997).

[24] W. Zhu, Y. Zhu, L. Wang, Q. Zhu, W.-H. Zhao, C. Zhu, J. Bai, J. Yang, L.-F. Yuan, H. Wu, and X. C. Zeng, Water confined in nanocapillaries: Two-dimensional bilayer squarelike ice and associated solid–liquid–solid transition, J. Phys. Chem. C **122**, 6704 (2018).

[25] O. F. Syljuåsen and M. B. Zvonarev, Directed-loop Monte Carlo simulations of vertex models, Phys. Rev. E **70**, 016118 (2004).

[26] M. Weigel and W. Janke, The square-lattice F model revisited: a loop-cluster update scaling study, J. Phys. A: Math. Gen. **38**, 7067 (2005).

[27] E. Ising, Beitrag zur Theorie des Ferromagnetismus, Z. Med. Phys. **31**, 253 (1925).

[28] F. Y. Wu, The Potts model, Rev. Mod. Phys. **54**, 235 (1982).

[29] H. Ma, W. Zhang, Y. Tian, C. Ding, and Y. Deng, Emergent topological ordered phase for the Ising-XY Model revealed by cluster-updating Monte-Carlo method, Chin. Phys. B **33**, 040503 (2024).

[30] R. Zhao, C. Ding, and Y. Deng, Overlap of two topological phases in the antiferromagnetic Potts model, Phys. Rev. E **97**, 052131 (2018).

[31] P. Belov and N. Reshetikhin, The two-point correlation function in the six-vertex model, J. Phys. A: Math. Theor. **55**, 155001 (2022).

[32] I. Lyberg, V. Korepin, and J. Viti, The density profile of the six vertex model with domain wall boundary conditions, J. Stat. Mech. (2017) 053103.

[33] K. Kubo, T. A. Kaplan, and J. R. Borysowicz, Monte Carlo simulation of the S=1/2 antiferromagnetic Heisenberg chain and the long-distance behavior of the spin-correlation function, Phys. Rev. B **38**, 11550 (1988).

[34] A. W. Sandvik, The directed-loop algorithm, *The Monte Carlo Method in the Physical Sciences: Celebrating the 50th Anniversary of the Metropolis Algorithm*, AIP Conf. Proc. No. 690 (AIP, New York, 2003), pp. 299–308.

[35] N. Prokof'ev, B. Svistunov, and I. Tupitsyn, "Worm" algorithm in quantum Monte Carlo simulations, Phys. Lett. A **238**, 253 (1998).

[36] N. Prokof'ev and B. Svistunov, Worm algorithms for classical statistical models, Phys. Rev. Lett. **87**, 160601 (2001).

[37] Y. Deng, T. M. Garoni, and A. D. Sokal, Dynamic critical behavior of the worm algorithm for the ising model, Phys. Rev. Lett. **99**, 110601 (2007).

[38] B.-Z. Wang, P. Hou, C.-J. Huang, and Y. Deng, Percolation of the two-dimensional XY model in the flow representation, Phys. Rev. E **103**, 062131 (2021).

[39] H. Chen, P. Hou, S. Fang, and Y. Deng, Monte Carlo study of duality and the Berezinskii-Kosterlitz-Thouless phase transitions of the two-dimensional q-state clock model in flow representations, Phys. Rev. E **106**, 024106 (2022).

[40] L. Zhang, M. Michel, E. M. Elçi, and Y. Deng, Loop-cluster coupling and algorithm for classical statistical models, Phys. Rev. Lett. **125**, 200603 (2020).

[41] Y.-J. Kao and R. G. Melko, Short-loop algorithm for quantum Monte Carlo simulations, Phys. Rev. E **77**, 036708 (2008).

[42] W. Zhang, L. Li, and W. Guo, Hard core bosons on the dual of the bowtie lattice, Phys. Rev. B **82**, 134536 (2010).

[43] W. Zhang, Y. Yang, L. Guo, C. Ding, and T. C. Scott, Trimer superfluid and supersolid on two-dimensional optical lattices, Phys. Rev. A **91**, 033613 (2015).

[44] W. Zhang, R. Li, W. X. Zhang, C. B. Duan, and T. C. Scott, Trimer superfluid induced by photoassocation on the state-dependent optical lattice, Phys. Rev. A **90**, 033622 (2014).

[45] W. Zhang, R. Yin, and Y. Wang, Pair supersolid with atom-pair hopping on the state-dependent triangular lattice, Phys. Rev. B **88**, 174515 (2013).

[46] T.-W. Chen, S.-D. Jheng, W.-F. Hsieh, and S.-C. Cheng, Vortex and trapped states of microcavity-polariton condensates in a harmonic trap, Comput. Mater. Sci. **117**, 579 (2016).

[47] K.-X. Xu, J.-H. Qiu, and L. yi Shi, Non-power-law I–V characteristics in Ca-doped polycrystalline $Y_{1-x}Ca_xBa_2Cu_3O_{7-\delta}$, Supercond. Sci. Technol. **19**, 178 (2006).

[48] H. Wei, J. Zhang, S. Greschner, T. C. Scott, and W. Zhang, Quantum Monte Carlo study of superradiant supersolid of light in the extended Jaynes-Cummings-Hubbard model, Phys. Rev. B **103**, 184501 (2021).

[49] O. Melchert, autoScale.py - A program for automatic finite-size scaling analyses: A user's guide, arXiv:0910.5403 [physics.comp-ph].

[50] Z. Wang, L. Feng, W. Zhang, and C. Ding, Phase transitions in a three-dimensional Ising model with cluster weight studied by Monte Carlo simulations, Phys. Rev. E **104**, 044132 (2021).

[51] G.-W. Chern, C. Reichhardt, and C. J. Olson Reichhardt, Frustrated colloidal ordering and fully packed loops in arrays of optical traps, Phys. Rev. E **87**, 062305 (2013).

[52] A. Ortiz-Ambriz and P. Tierno, Engineering of frustration in colloidal artificial ices realized on microfeatured grooved lattices, Nat. Commun. **7**, 10575 (2016).

[53] C. Nisoli, Unexpected phenomenology in particle-based ice absent in magnetic spin ice, Phys. Rev. Lett. **120**, 167205 (2018).

[54] A. Libál, C. Reichhardt, and C. J. O. Reichhardt, Realizing colloidal artificial ice on arrays of optical traps, Phys. Rev. Lett. **97**, 228302 (2006).

[55] C. J. Olson Reichhardt, A. Libál, and C. Reichhardt, Multi-step ordering in kagome and square artificial spin ice, New J. Phys. **14**, 025006 (2012).

[56] C. Nisoli, Dumping topological charges on neighbors: Ice manifolds for colloids and vortices, New J. Phys. **16**, 113049 (2014).

[57] A. Libál, C. J. O. Reichhardt, and C. Reichhardt, Creating artificial ice states using vortices in nanostructured superconductors, Phys. Rev. Lett. **102**, 237004 (2009).

[58] F. Ma, C. Reichhardt, W. Gan, C. J. O. Reichhardt, and W. S. Lew, Emergent geometric frustration of artificial magnetic skyrmion crystals, Phys. Rev. B **94**, 144405 (2016).

[59] C. Rodríguez-Gallo, A. Ortiz-Ambriz, and P. Tierno, Topological boundary constraints in artificial colloidal ice, Phys. Rev. Lett. **126**, 188001 (2021).

[60] A. Libál, D. Y. Lee, A. Ortiz-Ambriz, C. Reichhardt, C. J. O. Reichhardt, P. Tierno, and C. Nisoli, Ice rule fragility via topological charge transfer in artificial colloidal ice, Nat. Commun. **9**, 4146 (2018).

[61] C. Rodríguez-Gallo, A. Ortiz-Ambriz, C. Nisoli, and P. Tierno, Geometrical control of topological charge transfer in Shakti-Cairo colloidal ice, Commun. Phys. **6**, 113 (2023).

[62] Z. Y. Xie, H. C. Jiang, Q. N. Chen, Z. Y. Weng, and T. Xiang, Second renormalization of tensor-network states, Phys. Rev. Lett. **103**, 160601 (2009).

[63] L. Vanderstraeten, B. Vanhecke, and F. Verstraete, Residual entropies for three-dimensional frustrated spin systems with tensor networks, Phys. Rev. E **98**, 042145 (2018).